Volume 4 | Number 3 | May 2019 | Pages 543–770

Nanoscale Horizons

The home for rapid reports of exceptional significance in nanoscience and nanotechnology

rsc.li/nanoscale-horizons

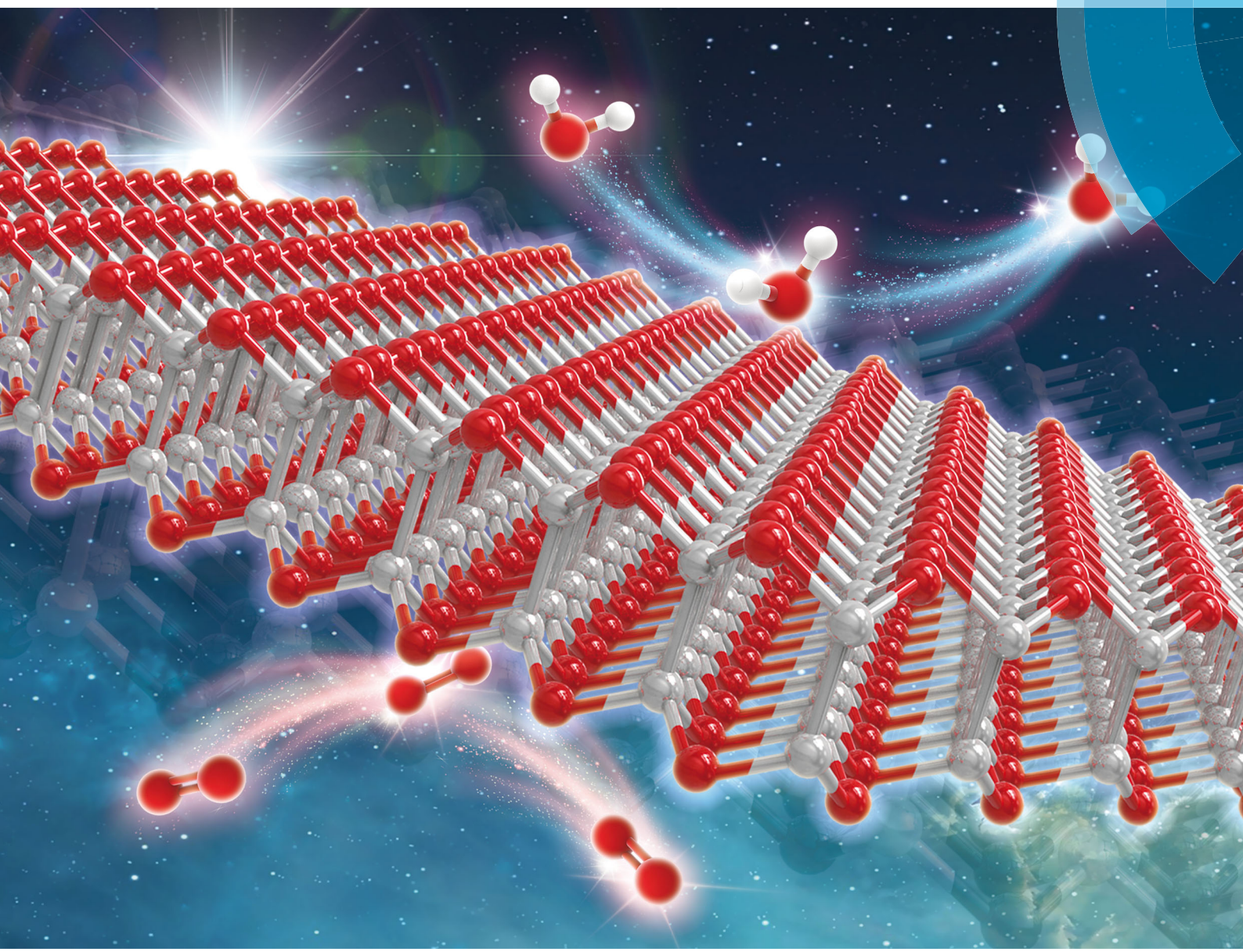

ISSN 2055-6756

ROYAL SOCIETY OF CHEMISTRY | Celebrating IYPT 2019

COMMUNICATION

Jijun Zhao, Xiao Cheng Zeng *et al.*

Eighteen functional monolayer metal oxides: wide bandgap semiconductors with superior oxidation resistance and ultrahigh carrier mobility

NCNST

Nanoscale Horizons

COMMUNICATION

View Article Online
View Journal | View Issue

Cite this: *Nanoscale Horiz.*, 2019, 4, 592

Received 30th August 2018,
Accepted 26th November 2018

DOI: 10.1039/c8nh00273h

rsc.li/nanoscale-horizons

Eighteen functional monolayer metal oxides: wide bandgap semiconductors with superior oxidation resistance and ultrahigh carrier mobility†

Yu Guo,[ab] Liang Ma,[b] Keke Mao,[bc] Minggang Ju,[b] Yizhen Bai,[a] Jijun Zhao *[a] and Xiao Cheng Zeng *[bd]

Layered metal oxides have emerged as an up-and-comer in the family of two-dimensional materials due to their natural abundance, intrinsic bandgap, and chemical inertness. Based on first-principles calculations, we systematically investigated the atomic structures, energetic stability, and electronic properties of 18 monolayer metal oxides. All these monolayer metal oxides are predicted to be energetically favorable with negative formation energies in the range of −4.27 to −0.47 eV per atom, suggesting good experimental feasibility for synthesis of these monolayer metal oxides. Monolayer metal oxides exhibit superior oxidation resistance, and possess modest to wide bandgaps (1.22–6.48 eV) and high carrier mobility (especially up to 8540 $cm^2 V^{-1} s^{-1}$ for the InO monolayer), thereby rendering these low-dimensional materials promising candidates for carrier transport. Also, a pronounced in-plane anisotropy for the carrier mobility with a longitudinal/horizontal ratio as large as 115 is revealed for the monolayer metal oxides. These 2D metal oxides exhibit notable absorption in the ultraviolet range with the absorption coefficient $>10^5$ cm^{-1}. The combined novel properties of these monolayer metal oxides offer a wide range of opportunities for advanced electronic and optoelectronic applications.

Conceptual insights

From systematical screening and unbiased particle-swarm optimization by first-principles calculations, we report eighteen stable 2D monolayer metal oxides. Among them, nine monolayer structures are predicted for the first time, and the others could be easily obtained by mechanical exfoliation from the layered bulk materials. All these monolayer metal oxides are promising 2D electronic and optoelectronic materials with superior chemical inertness, suitable bandgap in a wide range (1.22–6.48 eV), high carrier mobility up to 8540 $cm^2 V^{-1} s^{-1}$, and notable absorption in the ultraviolet region of nearly 10^6 cm^{-1}.

Introduction

Materials with open-air stability and superior carrier mobilities are highly desirable for applications in electronic and optoelectronic devices such as field-effect transistors (FETs), logic circuits and optical modulators.[1–3] The recently emerged two-dimensional (2D) materials have attracted intensive interest due to their novel physical properties, *e.g.*, high carrier mobility in certain 2D materials. However, not all 2D materials with high carrier mobility are suitable for advanced electronics. For example, despite the exceptionally high carrier mobilities of $\sim 10^5$ and $\sim 10^3$ $cm^2 V^{-1} s^{-1}$ for graphene and phosphorene,[3,4] respectively, the poor on/off ratio due to absence of a bandgap for graphene and the low open-air stability of phosphorene notably hinder their electronic and optoelectronic applications.[5,6] It is thus desirable to explore new functional 2D materials with high carrier mobility, moderate bandgap, and excellent open-air stability.

Metal oxides (MOs) are known wide bandgap (>2 eV) semiconductors with electron transition energy in the range of visible and ultraviolet light,[7–10] while exhibiting excellent reliability in harsh operating conditions.[11,12] Moreover, ZrO_2 and HfO_2 are known as high-*k* materials to replace the silicon dioxide gate dielectric layer of a microelectronic device.[13,14] Since many metal oxides are made from the abundant elements in the earth's crust, they are cost effective and often environmentally friendly. All these merits render the MOs promising for versatile applications.[7–10] Moreover, a number of MOs, such as MoO_3, TiO_2 and MnO_2, possess layered crystal structures with weak van der Waals (vdW) interaction between adjacent layers.[15,16] Thus, metal oxide sheets could be mechanically exfoliated from the bulk materials.[15,16] Furthermore, high carrier

[a] *Key Laboratory of Materials Modification by Laser, Ion and Electron Beams (Dalian University of Technology), Ministry of Education, Dalian, Liaoning 116024, China. E-mail: zhaojj@dlut.edu.cn*
[b] *Department of Chemistry, University of Nebraska–Lincoln, Lincoln, Nebraska 68588, USA. E-mail: xzeng1@unl.edu*
[c] *School of Energy and Environment Science, Anhui University of Technology, Maanshan, Anhui 243032, China*
[d] *Department of Chemical & Biomolecular Engineering and Department of Mechanical & Materials Engineering, University of Nebraska–Lincoln, Lincoln, Nebraska 68588, USA*

† Electronic supplementary information (ESI) available. See DOI: 10.1039/c8nh00273h

mobility was also revealed in layered MOs, *e.g.*, $\sim$1000 $cm^2 V^{-1} s^{-1}$ for MoO_3 flakes,[16] comparable to that of bulk silicon and 2D phosphorene.[4,17] Major advances of layered metal oxide films in electronic applications have already been achieved, including multigate FETs,[8,18] gas sensors,[18] p–n junctions and complementary circuits,[19,20] printable metal oxide electronics technology[21–23] and flat panel displays.[7,24] These findings and technological advancements indicate that the layered MOs represent an important class of 2D materials with great potential in cutting-edge electronics and optoelectronics.

To date, atomically thin films of MOs, including HfO_2, Al_2O_3, and Gd_2O_3, with the thickness down to 0.5 nm have been successfully fabricated in the laboratory.[10] Theoretically, the electronic properties of several monolayer metal oxides (MMOs), such as GeO, SnO, MoO_2, WO_2 and MoO_3, with different phases have been studied.[25–30] It was found that the bandgap of monolayer MOs decreases with increase of the thickness. Non-magnetic layered metal oxides could be transformed to magnetic ones with both sides of the layer being functionalized.[31,32] It was also found that Li and Na atoms can easily transport on the surface of MMOs with low diffusion barrier due to their weak binding with the MMOs,[32,33] demonstrating an advantage of MMOs as potential electrode materials in batteries. Moreover, an unexpected multiferroic phase was predicted for the SnO monolayer with a certain range of doped hole density.[34] The carrier mobility of monolayer MoO_3 could reach up to 3000 $cm^2 V^{-1} s^{-1}$,[29] suggesting that MoO_3 is a promising candidate in high-performance 2D electronic devices.

Although the electronic properties of several monolayer metal oxides with different phases have been studied previously, little is known about their carrier transport and optical properties. Based on systematical first-principles calculations, for the first time, we explore the atomic structures, energetic and chemical stability, and carrier transport properties of 18 monolayer metal oxides. All 18 MMOs entail negative formation energies, suggesting likelihood of synthesis in the laboratory. These MMOs exhibit superior oxidation resistance in the open-air environment. They also possess moderate to wide bandgaps (up to 6.48 eV), high carrier mobilities (up to $\sim$8540 $cm^2 V^{-1} s^{-1}$), pronounced in-plane anisotropy ratio of the carrier mobility (up to 115), and notable absorption coefficients in the ultraviolet wavelength region (up to 10^6 cm^{-1}). All these satisfactory properties render them promising candidates for carrier transport as well as for rectifier devices and ultraviolet photodetectors. Moreover, monolayer GeO, SnO, SnO-1, TiO_2, ZrO_2^T and HfO_2^T can be suitable as photocatalysts for water splitting. Our comprehensive study of the 2D MMO materials will promote future experimental efforts in exploration of these materials in 2D electronic and/or optoelectronic devices.

Results and discussion

Atomic structures and stability of monolayer metal oxides

The 18 monolayer metal oxides considered here share various lattice structures, including hexagonal structures in T and H phases, *e.g.*, ZrO_2^T, HfO_2^T, MoO_2^H, WO_2^H, NiO_2^T, PtO_2^T, InO, GeO_2^T, SnO_2^T and SnO_2^H, and orthorhombic structures for TiO_2, MoO_3, Mo_2O_5, WO_3, W_2O_5, GeO, SnO and SnO-1. The typical structures and corresponding lattice parameters are presented in Fig. S1 and Table S1 in the ESI,† respectively. The representative atomic structures with the lower energies are shown in Fig. 1 with the lattice parameters listed in Table 1. First, to assess the energetic stability of these MMOs, we calculate their formation energy ΔH defined as

$$\Delta H = (E_{tot} - n_1 \times E_M - n_2 \times E_O)/n \quad (1)$$

where E_{tot} is the energy of the MMOs; E_M and E_O are the energy of a metal in its solid phase and an oxygen atom in a gaseous O_2 molecule, respectively; n_1 and n_2 are the numbers of atoms for each element in the unit cell of MMO, and n is the total number of atoms in the unit cell. MMOs show negative ΔH of -0.47 to -4.27 eV per atom (see Table 1), indicating that the formation of MMOs is exothermic. For a material to be viewed as thermodynamically stable, it is necessary but not sufficient that $\Delta H < 0$. We calculate the energy of the MMOs with respect to the convex hull of competing bulk phases,[35] as shown in Fig. S2 (ESI†). The convex hull is currently constructed from the most stable binary bulk compounds of the MMOs. Clearly, most MMOs lie above the convex hull and are thus predicted to be thermodynamically metastable in their freestanding form under standard conditions. However, monolayer W_2O_5 and TiO_2 lie on the convex hull, indicating the thermodynamic stability of these two monolayers. The kinetic stability of these MMOs is confirmed by their phonon dispersions, as shown in Fig. S3 and S4 (ESI†). Although there are tiny imaginary branches (around -1.0 cm^{-1}) near the gamma point in their phonon dispersions, these imaginary frequencies could be removed by having higher numerical accuracy in total energy calculation and structural optimization, or by using larger supercells. Therefore, these MMOs are kinetically stable. We also performed Born–Oppenheimer molecular dynamics (BOMD) simulations to assess the thermal stability of MMOs (see Fig. S5, ESI†). The 10 ps BOMD simulations suggest that these MMOs can maintain their structure at least up to 500 K (except TiO_2 monolayer), indicating their good stability even above the room temperature.

To examine the chemical stability of MMOs in the open-air environment, we consider adsorption of an O_2 molecule on these 2D sheets. The interaction between O_2 and the MMO layer is described by the adsorption energy (E_{ad}) defined as:

$$E_{ad} = E_{ox} - E_{mono} - E_{O_2} \quad (2)$$

where E_{ox}, E_{mono} and E_{O_2} are the energies of an MMO sheet with an adsorbed O_2 molecule, the pristine MMO sheet, and an individual O_2 molecule in the triplet spin state, respectively. By definition, a positive E_{ad} means endothermic adsorption of an O_2 molecule. In particular, E_{ad} of O_2 adsorbed on these MMOs ranges from -0.091 eV to 0.271 eV (see Table 1). The weak or even positive adsorption energy indicates oxidation resistance of MMOs in the open-air environment. As shown in Fig. S6 (ESI†), E_{ad} with positive value increases when an initially physisorbed O_2 molecule gradually approaches monolayers

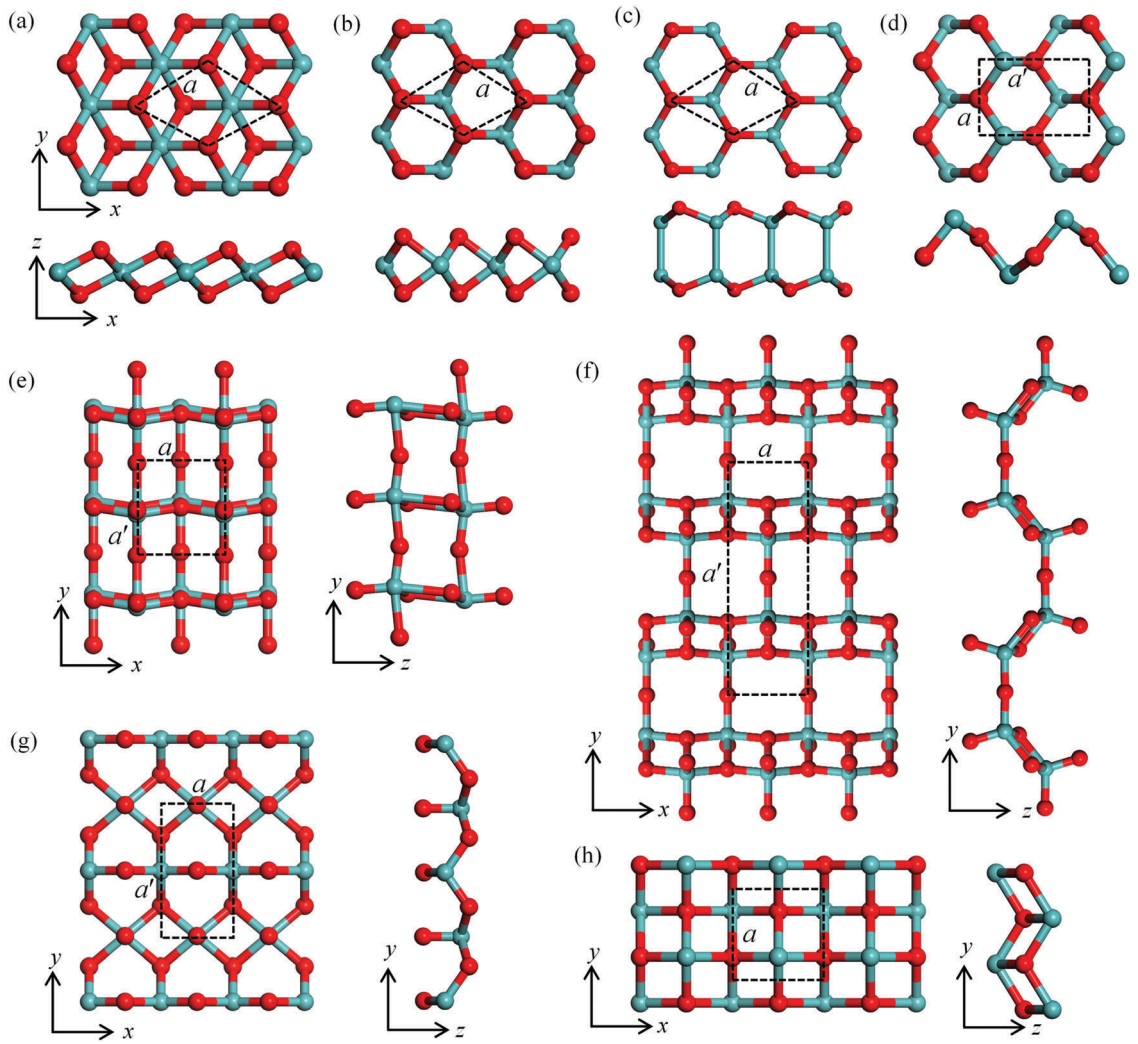

Fig. 1 The atomic structures of various monolayer metal oxides: (a) the hexagonal structures in the T phase for ZrO_2^T, HfO_2^T, NiO_2^T, PtO_2^T, GeO_2^T and SnO_2^T monolayers (the superscript "T" indicates T phase). (b) The hexagonal structures in the H phase including MoO_2^H, WO_2^H and SnO_2^H (the superscript "H" indicates H phase). (c), (e), (g) and (h) The structures of InO, MoO_3, TiO_2 and squared SnO-1 monolayers. (d) and (f) The monolayers of GeO and SnO, and Mo_2O_5 and W_2O_5, respectively. The top and bottom panels in (a), (b), (c) and (d) are top and side views, respectively. The left and right panels in (e), (f), (g) and (h) are top and side views, respectively. The lattice constants a/a' are highlighted by dashed lines. Metal and oxygen atoms are shown in green and red, respectively.

(taking InO or SnO_2^H monolayer as a representative), clearly showing the oxidation resistance of MMOs. The superior open-air stability of MMOs is a distinct advantage compared to many other 2D materials with poor chemical stability in an open-air environment. A well-known example is phosphorene, which can be easily oxidized in an air and moisture environment, with a low activation energy of 0.70 eV.[6] In turn, oxidation of phosphorene leads to higher contact resistance, lower carrier mobility, and possible mechanical degradation and breakdown.[36] Therefore, MMOs with superior oxidation resistance could sustain the device performance for long-term durability.

Knowledge of adsorption and dissociation of water on the surface of 2D materials is of crucial importance for evaluating the use of these metal oxides in humid air environment. To this end, we investigate H_2O adsorption and dissociation on MMOs [structure (d–h) in Fig. 1]. Here, we define the adsorption energy (E_{ad}*) to describe the interaction between H_2O and the MMO, as follows:

$$E_{ad}^{*} = E_{ox} - E_{mono} - E_{H_2O} \quad (3)$$

where E_{ox}, E_{mono} and E_{H_2O} are the energies of an MMO sheet with an adsorbed H_2O molecule, the pristine MMO sheet, and an individual H_2O molecule, respectively. By definition, a positive (negative) value means endothermic (exothermic) adsorption of a water molecule. As demonstrated in ESI† Fig. S7, for certain monolayers (*e.g.*, SnO, SnO-1, GeO, MoO_3, Mo_2O_5, WO_3, W_2O_5 and TiO_2), the adsorption energies of an H_2O molecule are in the range of −0.96 to −0.17 eV. For monolayer SnO, SnO-1, GeO, MoO_3 and WO_3 with smaller magnitude of adsorption energies (−0.28 to −0.17 eV), there is little charge transfer between the H_2O molecule and monolayers

Table 1 The calculated structural parameters (a/a') defined in Fig. 1, formation energy (ΔH), interlayer binding energy (E_B), bandgap (E_g), valence band maximum (VBM) and conduction band minimum (CBM) with vacuum level set at zero energy as the reference, adsorption energy (E_{ad}) of an oxygen molecule on metal oxide monolayer. "d" ("i") in the parentheses indicates a direct (indirect) bandgap

	a	ΔH	E_B	E_g	VBM	CBM	E_{ad}
Materials	Å	eV per atom		eV			
ZrO_2^T	3.29	−3.18	—	6.00 (i)	−9.07	−3.06	0.053
HfO_2^T	3.24	−3.36	—	6.48 (i)	−8.91	−2.43	−0.014
MoO_2^H	2.83	−1.87	—	1.74 (i)	−7.74	−6.00	0.271
WO_2^H	2.83	−1.94	—	2.16 (i)	−7.25	−5.09	0.003
NiO_2^T	2.83	−0.67	−0.001	3.09 (i)	−9.68	−6.59	0.031
PtO_2^T	3.16	−0.47	−0.002	3.47 (i)	−8.21	−4.74	−0.071
InO	3.48	−1.10	—	1.22 (i)	−7.26	−6.05	0.092
GeO_2^T	2.92	−1.51	—	5.17 (i)	−10.07	−4.90	0.202
SnO_2^T	3.22	−1.55	−0.004	4.11 (i)	−9.44	−5.32	0.028
SnO_2^H	3.10	−1.06	—	1.81 (i)	−9.56	−7.74	0.021
TiO_2	3.14/5.73	−4.27	−0.006	3.97 (d)	−8.37	−4.30	0.013
MoO_3	3.70/3.94	−1.80	−0.002	2.94 (i)	−9.54	−6.60	0.104
Mo_2O_5	3.83/11.11	−1.94	−0.003	1.36 (d)	−6.54	−5.18	0.002
WO_3	3.75/3.81	−2.06	—	2.35 (i)	−9.72	−7.37	0.003
W_2O_5	3.84/11.20	−3.68	−0.004	1.39 (d)	−6.03	−4.64	0.001
GeO	3.02/4.54	−1.16	—	3.73 (i)	−6.21	−2.47	−0.083
SnO	3.36/5.01	−1.26	−0.075	3.48 (i)	−5.47	−2.00	−0.002
SnO-1	3.84	−1.30	−0.037	3.92 (i)	−5.83	−1.90	−0.091

(see ESI† Fig. S8), indicating the weak adsorption of H_2O on these monolayers. Therefore, monolayer SnO, SnO-1, GeO, MoO_3 and WO_3 exhibit reasonable chemical inertness in the open-air environment.

Even the monolayers Mo_2O_5, W_2O_5 and TiO_2 yield H_2O adsorption energies as low as −0.96 eV; H_2O is not favored to dissociate into a H atom and a OH radical on the monolayers Mo_2O_5, W_2O_5 and TiO_2 due to the positive adsorption energy in the range of 1.04–3.05 eV and negative reaction of heat (defined as the energy difference between initial and final states) in the range of −4.01 to −1.63 eV, as shown in Fig. S9 and Table S2 (ESI†). Only TiO_2 can easily dissociate H_2O into two separated H atoms and one oxygen atom with an exothermic heat of reaction of −0.56 eV. ESI† Fig. S10 illustrates the path for H_2O dissociation on the monolayer TiO_2. Although the reaction is exothermic, the H_2O molecule undergoes a transition to three atoms by overcoming a high activation barrier of 1.84 eV, suggesting a slow rate of H_2O dissociation, and modest chemical stability of the monolayer TiO_2 in ambient air.

Since the 2D monolayer or few-layer materials are usually fabricated by mechanical exfoliation from their bulk solids, we calculate the interlayer binding energy to assess the ability for exfoliation from bulk counterparts. We define the interlayer binding energy E_B as follows:

$$E_B = (E_{bulk} - n_1 \times E_{ML})/n_2 \quad (4)$$

where E_{bulk} and E_{ML} are the total energies of bulk and monolayer metal oxides in the unit cell, respectively; n_1 is the number of layers in the bulk structures; n_2 is the total number of atoms in the unit cell of bulk metal oxides. Since the bulk phases of NiO_2^T, PtO_2^T, SnO_2^T, TiO_2, MoO_3, Mo_2O_5, W_2O_5, SnO and SnO-1 exhibit layered structures,[37,38] the monolayers of these systems could be obtained directly by mechanical exfoliation.[39] As displayed in Table 1, the calculated binding energies of two monolayers are in the range of −0.001 and −0.075 eV per atom, comparable to or even less than those of two phosphorene (−0.055 eV per atom),[40] graphene and h-BN sheets (both around −0.065 eV per atom).[41] These results demonstrate high possibility of exfoliating MMOs from the layered bulk solids.

Electronic structures and carrier transport properties of monolayer metal oxides

Previously, the geometric and electronic structures of monolayer GeO, SnO, SnO_2, MoO_2, WO_2, MoO_3 and NiO_2 were studied,[25–30] but the carrier mobilities of only MoO_3 and SnO monolayers were reported.[27,29] Here, the carrier transport properties of the MMOs are systematically investigated. The electronic band structures of the MMOs are presented in Fig. 2, and their bandgaps are given in Table 1. All 18 MMOs are either semiconductors or insulators, with bandgaps ranging from 1.22 to 6.48 eV, which are comparable to the values of other wide band-gap semiconducting 2D materials, like boron monochalcogenides (with bandgap in the range of 2.06–4.00 eV).[42] In particular, TiO_2, Mo_2O_5 and W_2O_5 monolayers possess a direct bandgap. At the HSE06 level of theory, the majority of MMOs considered here, including WO_2^H, NiO_2^T, PtO_2^T, GeO_2^T, SnO_2^T, TiO_2, MoO_3, WO_3, GeO, SnO and SnO-1 monolayers, are wide bandgap semiconductors with 5.17 eV > E_g > 2 eV. Thus, these MMOs are suitable for potential applications as electronic and optoelectronic devices to operate at much higher voltages, frequencies and temperatures than the conventional semiconductor materials like silicon and gallium arsenide.[43–46] On the other hand, ZrO_2 and HfO_2 monolayers possess exceptionally large bandgaps of 6.0 and 6.48 eV, and should be considered as 2D insulators. Their carrier transport properties will not be discussed below. Nevertheless, the large bandgaps for monolayer ZrO_2 and HfO_2 render their possible application in ultraviolet photodetectors.[47–49]

Based on the band structures shown in Fig. 2, the effective masses of carriers for 16 MMOs are calculated and summarized in Table 2. The effective masses are in the range of 0.73–6.73 m_0 (0.73–4.52 m_0) for holes, and 0.31–6.12 m_0 (0.10–6.74 m_0) for electrons along the x direction (y direction), respectively. Moreover, MoO_2^H, WO_2^H, PtO_2^T, W_2O_5 and SnO monolayers (SnO_2^T, SnO_2^H, TiO_2, MoO_3, WO_3 and GeO monolayers) exhibit strong directional anisotropy with a longitudinal/horizontal ratio up to 18.4 for electrons (5.1 for holes). The carrier effective mass in this work is distinct from that in ref. 35 since the unit cell or supercell adopted is different, hence the x-direction of the effective mass. The monolayer metal oxides as a photocatalyst for water splitting are demonstrated in ESI,† S7. By comparing the band edges with the redox potentials of water, we identified that monolayer TiO_2, GeO, SnO, SnO-1, ZrO_2^T and HfO_2^T can be potential functional photocatalysts for water splitting at acidic or neutral environments. However, considering the overpotentials for oxygen and hydrogen evolution processes,[50] only the GeO monolayer satisfies the basic requirement for water splitting.

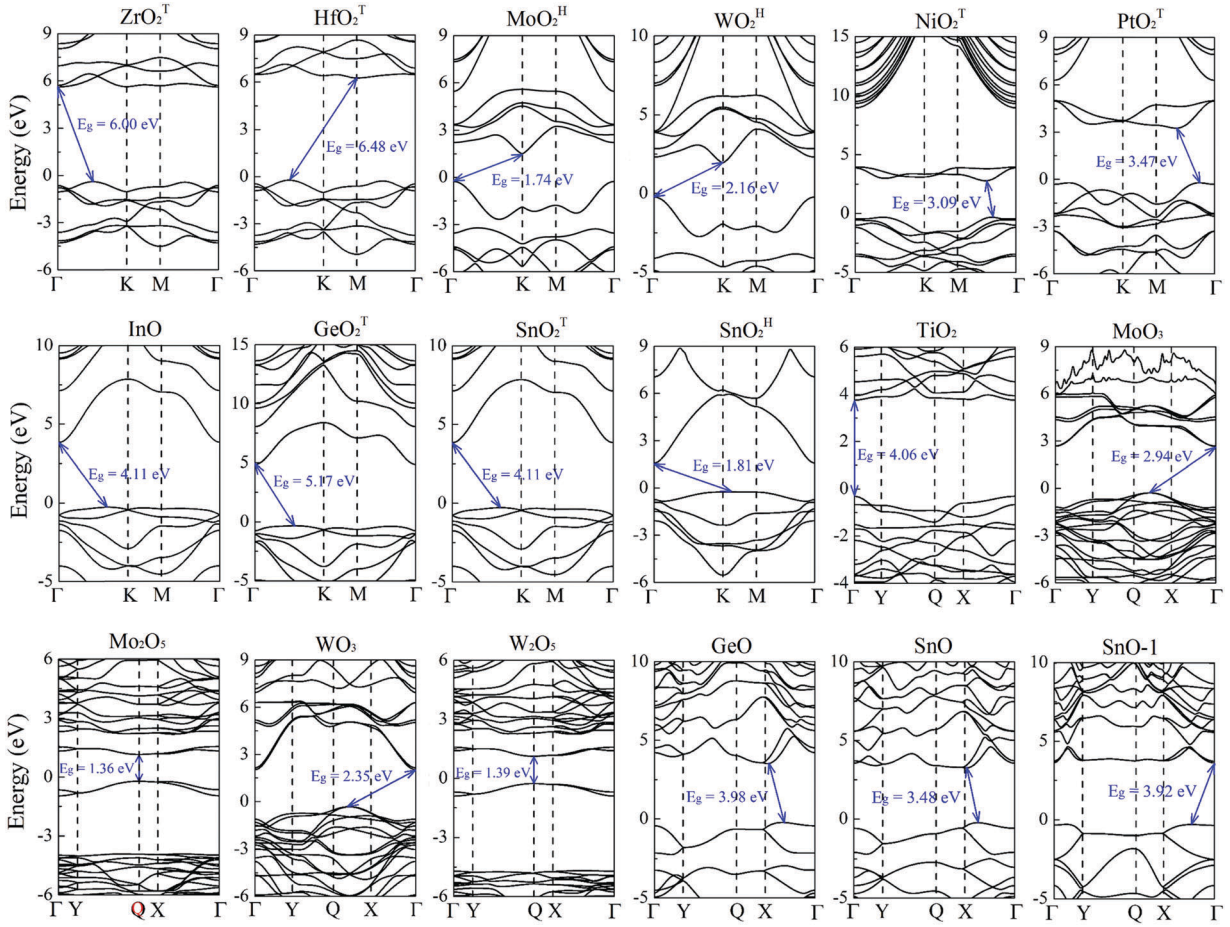

Fig. 2 Electronic band structures of monolayer metal oxides based on the HSE06 functional. E_g is the band gap denoted by the solid blue arrow. High-symmetry points in the first Brillouin zone are Γ (0, 0, 0), K (−0.333, 0.666, 0) and M (0, 0.5, 0) for hexagonal structures, and Γ (0, 0, 0), Y (0, 0.5, 0), Q (0.5, 0.5, 0) and X (0.5, 0, 0) for orthorhombic structures, respectively.

Table 2 Effective mass m^h of hole carriers, deformation potential constant E_1, elastic modulus C and hole mobility μ^h for monolayer metal oxides. m_0 is the electron rest mass. The subscripts x and y represent the directions defined in Fig. 1

	m_x^h	m_y^h	E_{1x}	E_{1y}	C_x	C_y	μ_x^h	μ_y^h
Materials	m_0		eV		J m^{-2}		cm^2 V^{-1} s^{-1}	
MoO_2^H	0.75	0.75	15.20	15.19	253.73	238.05	41.17	38.71
WO_2^H	0.73	0.73	4.97	5.50	284.37	289.63	455.89	379.18
NiO_2^T	1.96	2.01	1.39	1.53	141.77	144.29	399.26	326.01
PtO_2^T	1.34	1.33	9.14	2.11	118.29	126.51	16.64	338.89
InO	2.81	2.68	4.91	5.14	100.44	103.51	11.40	11.21
GeO_2^T	3.92	3.80	4.37	4.85	175.40	175.85	12.80	10.75
SnO_2^T	6.73	3.07	5.85	5.68	151.70	152.76	3.05	7.14
SnO_2^H	3.35	5.81	3.17	3.53	159.49	169.41	22.60	11.18
TiO_2	4.46	0.88	3.17	2.67	104.21	85.02	24.75	145.12
MoO_3	2.91	0.91	1.07	6.50	178.65	150.01	698.56	50.78
Mo_2O_5	2.30	2.27	0.66	1.81	91.36	10.79	853.92	13.36
WO_3	2.91	1.52	7.46	10.16	197.75	198.13	12.25	12.63
W_2O_5	3.99	3.07	3.48	3.20	117.09	17.54	14.60	3.37
GeO	2.63	1.16	0.73	1.37	44.79	46.78	385.03	256.97
SnO	1.34	1.73	0.79	1.46	60.04	15.46	990.93	58.10
SnO-1	3.51	3.51	2.10	2.10	40.73	40.73	15.30	15.30

To further estimate the carrier transport properties of MMOs, we calculate their acoustic phonon-limited carrier mobility μ based on the Takagi model within the deformation potential approximation:[51,52]

$$\mu = \frac{e\hbar^3 C_{2D}}{k_B T m m_d (E_{1,i})^2} \quad (5)$$

where e is the electron charge; $\hbar$ is the reduced Planck constant; k_B is the Boltzmann constant; T is the temperature; m is the effective mass along the transport direction; $m_d = \sqrt{m m_\perp}$ is the average effective mass ($m_\perp$ is the effective mass perpendicular to the transport direction); C_{2D} is the elastic modulus of the 2D sheet, determined by varying the lattice parameter l along the transport direction *via* $\Delta E/S_0 = C_{2D}(\Delta l/l)^2/2$ (ΔE is the energy change of the system under lattice deformation Δl, S_0 is the area of the 2D sheet); the term $E_{1,i}$ represents the deformation potential constant of the valence band maximum (VBM) for a hole or the conduction band minimum (CBM) for an electron along the transport direction, defined by $\Delta V/(\Delta l/l)$ (ΔV is the band edge shift under lattice deformation). All data are calculated using a strain step of 0.5%. The temperature considered

Table 3 Effective mass m^e of electron carriers, deformation potential constant E_1, elastic modulus C and hole mobility μ^e for monolayer metal oxides. The subscripts x and y represent the directions defined in Fig. 1

	m_x^e	m_y^e	E_{1x}	E_{1y}	C_x	C_y	μ_x^e	μ_y^e
Materials	m_0		eV		J m^{-2}		cm^2 V^{-1} s^{-1}	
MoO_2^H	6.12	0.46	10.22	3.37	253.73	238.05	5.01	579.88
WO_2^H	7.00	0.38	7.18	7.94	284.37	289.63	10.13	153.68
NiO_2^T	0.78	0.98	2.72	3.41	141.77	144.29	597.75	306.19
PtO_2^T	1.05	6.74	7.06	2.92	118.29	126.51	17.85	17.36
InO	0.33	0.10	2.47	3.76	100.44	103.51	5915.33	8540.85
GeO_2^T	0.36	0.36	8.59	8.69	175.40	175.84	386.01	378.14
SnO_2^T	0.37	0.37	2.68	2.91	151.70	152.76	3262.75	2797.24
SnO_2^H	0.31	0.31	3.10	2.96	159.49	169.41	3563.53	4150.41
TiO_2	2.43	3.11	7.21	2.44	104.21	85.02	6.31	24.75
MoO_3	0.80	0.56	2.15	11.62	178.65	150.01	1466.35	61.86
Mo_2O_5	4.28	3.66	0.50	1.72	91.36	10.79	454.00	5.32
WO_3	0.80	0.57	5.31	8.94	197.75	198.13	264.03	133.57
W_2O_5	2.08	3.96	1.54	2.65	117.09	17.54	175.24	4.64
GeO	0.41	1.74	4.34	0.50	44.79	46.78	144.29	2684.25
SnO	0.38	1.41	3.90	0.36	60.04	15.46	294.55	2473.65
SnO-1	0.42	0.42	3.26	3.26	40.73	40.73	444.10	444.10

in the mobility calculations is 300 K. The present carrier mobility calculation has been evidenced to be not only computationally efficient but also physically reasonable.[53,54]

The mobilities of electrons and holes calculated by the HSE06 functional are given in Table 3 and schematically shown in Fig. 3. At first glance, the mobilities of electrons ranging from 4.46 to 8541 cm^2 V^{-1} s^{-1} are substantially larger than those of holes (3.37–990.93 cm^2 V^{-1} s^{-1}). Also note that the carrier mobility shows rather pronounced anisotropy with large longitudinal/horizontal ratio up to 115 (see Table S3, ESI†). This feature could be utilized to enhance the device performance by controlling the direction of carrier transport. Generally speaking, the carrier mobilities of most MMOs are in the order of magnitude of hundreds of cm^2 V^{-1} s^{-1}, which is comparable with those of common 2D materials like phosphorene and MoS_2.[53,55] More importantly, five monolayers of InO, SnO_2^T, TiO_2, MoO_3, SnO and GeO exhibit outstanding electron mobilities above 1000 cm^2 V^{-1} s^{-1} and even reach up to 8540 cm^2 V^{-1} s^{-1} for InO, implying that MMOs should be promising candidates for high-speed electronic devices. Our present results, taking MoO_3 monolayer as a representative (1466 and 61.86 cm^2 V^{-1} s^{-1} for electrons, and 698.56 and 50.78 cm^2 V^{-1} s^{-1} for holes along x and y directions, respectively), are in good agreement with previous theoretical values (1608.80 and 37.52 cm^2 V^{-1} s^{-1} for electrons, and 800.57 and 25.56 cm^2 V^{-1} s^{-1} for holes along x and y directions, respectively).[29] The 2D elastic contant (C_{2D}) is attained by a quadratic fitting of the total energy *versus* strain (Fig. S11, ESI†) and the deformation potential constant ($E_{1,i}$) is calculated by the linear fitting of the CBM (VBM)–strain relation (Fig. S12, ESI†). Furthermore, electronic properties of MMOs containing heavy elements (Hf, Pt, W) are calculated by considering spin–orbit coupling, as displayed in Fig. S13 and Table S4 (ESI†). The results show that electonic properties, including the bandgap, carrier effective mass, deformation potential and carrier mobility, are little influenced by the spin–orbit coupling. For example, after inclusion of the spin–orbit coupling effect, the bandgaps and carrier mobilities change only slightly by 0.03–0.05 eV and 2–40 cm^2 V^{-1} s^{-1}, respectively. Similarly, the electronic properties of MMOs are calculated by using the DFT+U method with Hubbard U parameters of 2.0 eV for Hf, 4.8 eV for Mo, 6.2 eV for W, 5.1 eV for Ni, 3.0 eV for Pt, and 4.2 eV for Ti.[38,55–58] The results indicate that the Coulomb interaction results in changes of 0.06–0.25 eV

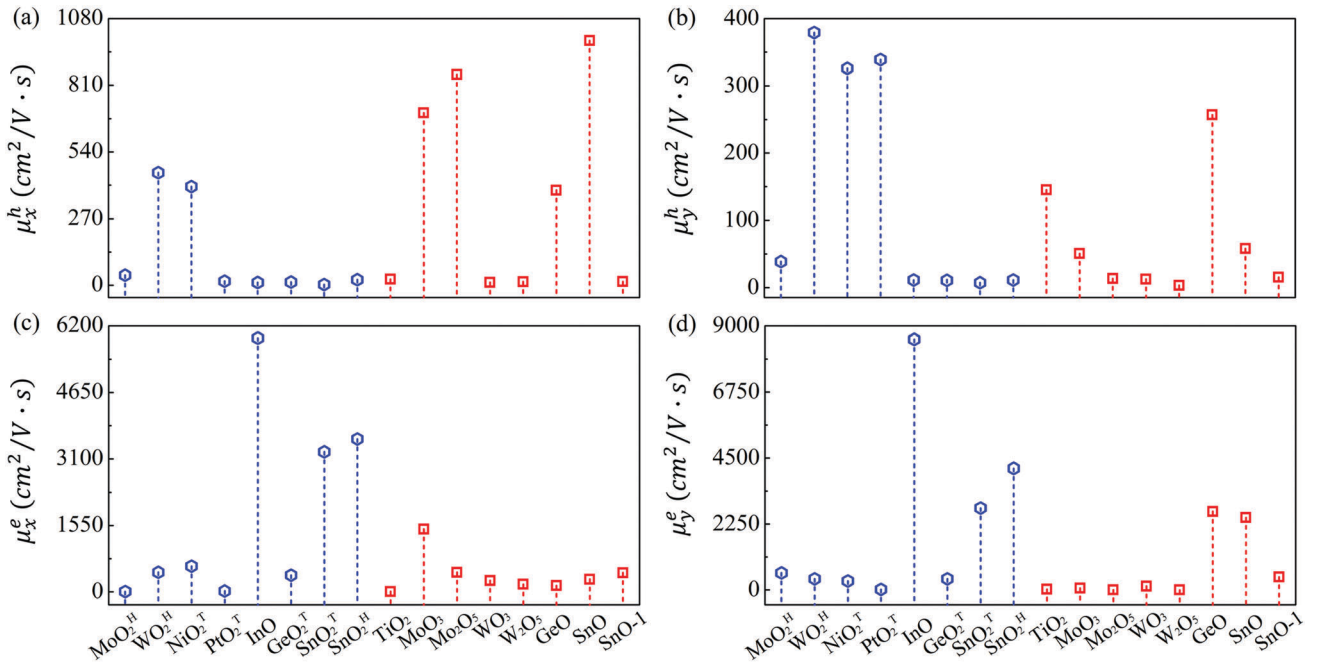

Fig. 3 Computed carrier mobility of (a) and (b) holes, and (c) and (d) electrons along the x and y directions. The blue hexagonal and red squares indicate 2D hexagonal and orthorhombic lattice structures, respectively.

for the band gaps, compared with the values of HSE06 calculation. Meanwhile, carrier mobilities calculated by using the DFT+U method range from 6.89 to 1784.39 $cm^2\ V^{-1}\ s^{-1}$, a similar trend as calculated by using the HSE06 functional (see Fig. S14 and Table S5, ESI†).

Since the experimentally synthesized metal oxide sheets could be multilayer rather than monolayer, we calculate the carrier mobilities of InO bilayer and trilayer. As given in Table S6 (ESI†), multilayer InO sheets still retain ultrahigh carrier mobility up to 7490 $cm^2\ V^{-1}\ s^{-1}$, rather close to 8540 $cm^2\ V^{-1}\ s^{-1}$ for InO monolayer. Our results indicate that layered metal oxides hold great promise for the next-generation 2D electronic devices. The high carrier mobility of the 2D metal oxides can be attributed to their relatively small effective mass, large elastic modulus, and small deformation potential constant. These systems show large C_{2D} values up to 290 $J\ m^{-2}$, approaching the value of graphene (330 $J\ m^{-2}$). In these stiff sheets, the acoustic phonons possess a large group velocity, leading to the small amplitude of lattice waves and weak scattering with charge carriers. The deformation potential constant $E_{1,i}$ is another important factor for carrier mobility. It approximates the strength of electron–phonon coupling and is determined by the band edge shift under lattice variation due to acoustic phonons. $E_{1,i}$ for MMOs could be as low as 0.36 eV, comparable with 0.15 eV of phosphorene,[53] which is able to significantly promote the carrier mobility.

Optical absorption properties of monolayer metal oxides

Semiconductors with wide bandgaps can serve as potential visible-blind ultraviolet photodetectors. To this end, we computed optical absorption coefficients of several MMOs with wide bandgap in the ultraviolet region (*i.e.*, wavelength from 10 nm to 400 nm), as shown in Fig. 4 and Fig. S15 (ESI†). Mostly, the optical absorption coefficients can reach as high as $10^5\ cm^{-1}$, comparable to that of zincblende, rock salt and wurtzite AlN.[43,59] The majority of MMOs exhibit outstanding optical adsorption properties at far ultraviolet (wavelength range of 122–200 nm). In particular, the optical absorption coefficient of ZrO_2^T monolayer exhibits a value of nearly $10^6\ cm^{-1}$ at a wavelength of ~69 nm. Prototype devices of ultraviolet detectors made up of h-BN and group-IV chalcogenide sheets have been demonstrated in previous experiments.[60–62] The h-BN based deep ultraviolet optical sensor showed very good response to ultraviolet light with wavelengths below 254 nm.[63] The detector by group-IV chalcogenide films (such as SnS_2) exhibited a remarkable photoresponse above 300 nm, dependence of photocurrent on optical power and wavelength, fast-response, and excellent photo-switch and long-term stability.[64,65] By analogy, the present monolayer MMOs with wide bandgap could be promising functional materials for ultraviolet detectors.

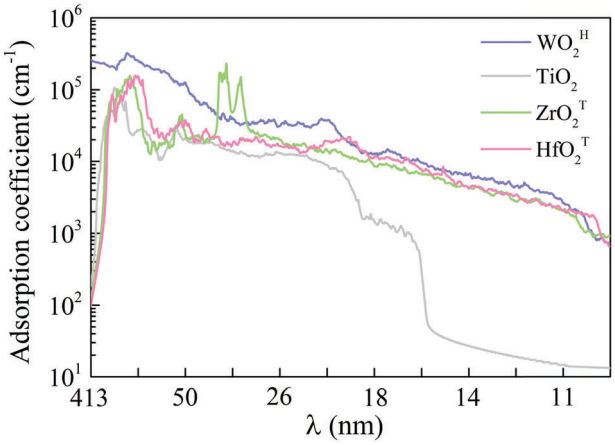

Fig. 4 Optical absorption coefficients in the ultraviolet wavelength region for monolayer WO_2^H, TiO_2, ZrO_2^T and HfO_2^T. λ is the wavelength.

Conclusion

We have theoretically explored the atomic structures, energetic stability, electronic and optical properties of 18 monolayer metal oxides. Among them, the most stable structures of 9 monolayer metal oxides are predicted from the unbiased particle-swarm optimization while structures of the other 9 monolayer metal oxides can be simply exfoliated from the bulk counterparts. All 18 monolayer metal oxides are energetically favorable with negative formation energies of −4.27 to −0.47 eV per atom, suggesting high experimental feasibility for the synthesis or mechanical exfoliation of the monolayers. Many of these monolayer metal oxides are wide bandgap semiconductors with chemical inertness, and some entail high carrier mobility up to 8540 $cm^2\ V^{-1}\ s^{-1}$ as well as pronounced in-plane anisotropy of the carrier mobility with large longitudinal/horizontal ratio up to 115. Moreover, the computed band gaps and band edge positions of monolayer TiO_2, GeO, SnO, SnO-1, ZrO_2^T and HfO_2^T suggest their potential applications as functional photocatalysts for water splitting at acidic or neutral environments. Several monolayer metal oxides also exhibit notable absorption spectra in the ultraviolet wavelength region, with adsorption coefficients above $10^5\ cm^{-1}$. Hence, these monolayer metal oxides with band gaps in the range of 1.22–6.48 eV may serve as functional 2D materials in visible light or ultraviolet photodetectors, as well as high-temperature and high-power electronic devices for electron and hole transport.

Computational methods

Density functional theory (DFT) calculations[66] were performed by using the Vienna ab initio simulation package 5.4.[67] More specifically, we used the planewave basis set with an energy cutoff of 500 eV,[68] the projector augmented wave (PAW) potentials,[69] and the generalized gradient approximation parameterized by Perdew, Burke and Ernzerhof (PBE) for the exchange–correlation functional.[70] Since the conventional GGA functional like PBE tends to underestimate the band gaps, a hybrid functional (HSE06) was used to compute the electronic structures and optical properties of the 18 metal oxide sheets. The convergence criterion of total energy was set to 10^{-7} eV. The geometry optimization was considered to be successful when the residual force on each

atom was less than 0.01 eV $Å^{-1}$. Uniform *k*-point meshes with spacing of $\sim$0.015 $Å^{-1}$ were adopted to sample the 2D Brillouin zones. A vacuum region of 15 Å was added to the vertical direction to avoid interactions between the neighboring layers. The Grimme's DFT-D3 scheme[71] was adopted to describe the long-range vdW interactions for computing the interlayer cohesive energy and O_2 adsorption energy. Phonon dispersion analysis was performed by using the Phonopy code[72] interfaced with the density functional perturbation theory (DFPT) as implemented in VASP.[73]

In total, 18 monolayer metal oxides were considered in this work – M_xO_y (M = Zr, Hf, Mo, W, Ni, Pt, In, Ge and Sn; x = 1, 2; y = 1, 2, 3, 5). Since bulk NiO_2^T, PtO_2^T, SnO_2^T (the superscript "T" indicates T phase[74]), TiO_2, MoO_3, Mo_2O_5, W_2O_5, SnO and SnO-1 exhibit layered structures,[37,38] their monolayer sheets could be obtained *via* mechanical exfoliation. For these systems, we can simply take a monolayer from the corresponding bulk crystal as the initial structure. For MoO_2^H, WO_2^H, InO, GeO_2^T, SnO_2^H, WO_3, GeO, ZrO_2^T and HfO_2^T (the superscript "H" indicates H phase[75]), we employed the particle-swarm optimization (PSO) method as implemented in CALYPSO code,[76,77] to seek the most stable monolayer structures. As a global optimization method, the PSO algorithm has been successfully used to predict many stable structures of 2D materials.[78–80] In our PSO search, the population size was set to 30, and the number of generations was maintained at 30. The required structural relaxations were performed by using the PBE functional, implemented in VASP 5.4 code.

Conflicts of interest

There are no conflicts to declare.

Acknowledgements

This work was supported by Science Challenge Project (TZ2018004), the National Natural Science Foundation of China (11574040, 21803002), and the Fundamental Research Funds for the Central Universities of China (DUT17LAB19). Y. G. is supported by China Scholarship Council (CSC 201706060138). We acknowledge the computing resources from the Supercomputing Center of Dalian University of Technology and the University of Nebraska Holland Computing Center.

References

1 Y. Pan, L. Zhang, L. Huang, L. Li, L. Meng, M. Gao, Q. Huan, X. Lin, Y. Wang, S. Du, H.-J. Freund and H.-J. Gao, *Small*, 2014, **10**, 2215–2225.
2 Z. Sun, A. Martinez and F. Wang, *Nat. Photonics*, 2016, **10**, 227.
3 K. S. Novoselov, A. K. Geim, S. V. Morozov, D. Jiang, Y. Zhang, S. V. Dubonos, I. V. Grigorieva and A. A. Firsov, *Science*, 2004, **306**, 666.
4 L. Li, Y. Yu, G. J. Ye, Q. Ge, X. Ou, H. Wu, D. Feng, X. H. Chen and Y. Zhang, *Nat. Nanotechnol.*, 2014, **9**, 372.
5 K. Novoselov, *Nat. Mater.*, 2007, **6**, 720.
6 Y. Guo, S. Zhou, Y. Bai and J. Zhao, *ACS Appl. Mater. Interfaces*, 2017, **9**, 12013–12020.
7 X. Yu, T. J. Marks and A. Facchetti, *Nat. Mater.*, 2016, **15**, 383.
8 I. Ferain, C. A. Colinge and J.-P. Colinge, *Nature*, 2011, **479**, 310.
9 M.-G. Kim, M. G. Kanatzidis, A. Facchetti and T. J. Marks, *Nat. Mater.*, 2011, **10**, 382.
10 A. Zavabeti, J. Z. Ou, B. J. Carey, N. Syed, R. Orrell-Trigg, E. L. H. Mayes, C. Xu, O. Kavehei, A. P. O'Mullane, R. B. Kaner, K. Kalantar-zadeh and T. Daeneke, *Science*, 2017, **358**, 332.
11 J. You, C.-C. Chen, L. Dou, S. Murase, H.-S. Duan, S. A. Hawks, T. Xu, H. J. Son, L. Yu, G. Li and Y. Yang, *Adv. Mater.*, 2012, **24**, 5267–5272.
12 K. An, Q. Zhang, S. Alayoglu, N. Musselwhite, J.-Y. Shin and G. A. Somorjai, *Nano Lett.*, 2014, **14**, 4907–4912.
13 W. He, W. Xu, Q. Peng, C. Liu, G. Zhou, S. Wu, M. Zeng, Z. Zhang, J. Gao, X. Gao, X. Lu and J. M. Liu, *J. Phys. Chem. C*, 2016, **120**, 9949–9957.
14 M. Gutowski, J. E. Jaffe, C.-L. Liu, M. Stoker, R. I. Hegde, R. S. Rai and P. J. Tobin, *Appl. Phys. Lett.*, 2002, **80**, 1897–1899.
15 L. Wang and T. Sasaki, *Chem. Rev.*, 2014, **114**, 9455–9486.
16 S. Balendhran, J. Deng, J. Z. Ou, S. Walia, J. Scott, J. Tang, K. L. Wang, M. R. Field, S. Russo, S. Zhuiykov, M. S. Strano, N. Medhekar, S. Sriram, M. Bhaskaran and K. Kalantar-zadeh, *Adv. Mater.*, 2013, **25**, 109–114.
17 N. D. Arora, J. R. Hauser and D. J. Roulston, *IEEE Trans. Electron Devices*, 1982, **29**, 292–295.
18 Y. C. Song, Y. H. Kang, J. Y. Jung, S. Y. Nam, J. Lim, S. C. Yoon, H. C. Dong and C. Lee, *Chem. Mater.*, 2012, **24**, 3517–3524.
19 H. Huang, H. Gong, C. L. Chow, J. Guo, T. J. White, M. S. Tse and O. K. Tan, *Adv. Funct. Mater.*, 2011, **21**, 2680–2686.
20 M. Tadatsugu, N. Yuki and M. Toshihiro, *Appl. Phys. Express*, 2013, **6**, 044101.
21 Y. Choi, G. H. Kim, W. H. Jeong, H. J. Kim, B. D. Chin and J.-W. Yu, *Thin Solid Films*, 2010, **518**, 6249–6252.
22 D. Spiehl, M. Häming, H. M. Sauer, K. Bonrad and E. Dörsam, *IEEE Trans. Electron Devices*, 2015, **62**, 2871–2877.
23 J. Leppäniemi, O.-H. Huttunen, H. Majumdar and A. Alastalo, *Adv. Mater.*, 2015, **27**, 7168–7175.
24 U. Betz, M. Kharrazi Olsson, J. Marthy, M. F. Escolá and F. Atamny, *Surf. Coat. Technol.*, 2006, **200**, 5751–5759.
25 J. A. Reyes-Retana and F. Cervantes-Sodi, *Sci. Rep.*, 2016, **6**, 24093.
26 C. Kamal, A. Chakrabarti and M. Ezawa, *Phys. Rev. B*, 2016, **93**, 125428.
27 J. Du, C. Xia, Y. Liu, X. Li, Y. Peng and S. Wei, *Appl. Surf. Sci.*, 2017, **401**, 114–119.
28 W.-Z. Xiao, G. Xiao and L.-L. Wang, *J. Chem. Phys.*, 2016, **145**, 174702.
29 W. B. Zhang, Q. Qu and K. Lai, *ACS Appl. Mater. Interfaces*, 2017, **9**, 1702–1709.
30 F. Haque, T. Daeneke, K. Kalantar-zadeh and J. Z. Ou, *Nano-Micro Lett.*, 2017, **10**, 23.
31 J. Tao and L. Guan, *Sci. Rep.*, 2017, **7**, 44568.
32 F. Li and Z. Chen, *Nanoscale*, 2013, **5**, 5321–5333.
33 C. C. Leong, H. Pan and S. K. Ho, *Phys. Chem. Chem. Phys.*, 2016, **18**, 7527–7534.

34 L. Seixas, A. S. Rodin, A. Carvalho and A. H. C. Neto, *Phys. Rev. Lett.*, 2016, **116**, 206803.
35 H. Sten, S. Mikkel, P. Mohnish, D. Thorsten, S. S. Per, F. H. Nicki, N. G. Morten, T. Daniele, M. L. Peter, C. R.-J. Anders, G. Jakob, W. J. Karsten, M. Jens Jørgen, O. Thomas and S. T. Kristian, *2D Mater.*, 2018, **5**, 042002.
36 A. Ziletti, A. Carvalho, D. K. Campbell, D. F. Coker and A.H. Castro Neto, *Phys. Rev. Lett.*, 2015, **114**, 046801.
37 L. C. P. Villars, *American Society of Metals*, Cleveland, OH, 1985.
38 K. Persson, https://materialsproject.org/.
39 H. Peelaers and C G. V. d. Walle, *J. Phys.: Condens. Matter*, 2014, **26**, 305502.
40 Y. Cai, G. Zhang and Y.-W. Zhang, *Sci. Rep.*, 2014, **4**, 6677.
41 G. Gabriella, K. Jiří, F.-A. Felix and M. Angelos, *J. Phys.: Condens. Matter*, 2012, **24**, 424216.
42 B. Mortazavi and T. Rabczuk, *Energies*, 2018, **11**, 1573.
43 E. Monroy, F. Omnès and F. Calle, *Semicond. Sci. Technol.*, 2003, **18**, R33.
44 J. L. Hudgins, G. S. Simin, E. Santi and M. A. Khan, *IEEE Trans. Power Electron.*, 2003, **18**, 907–914.
45 P. G. Neudeck, R. S. Okojie and C. Liang-Yu, *Proc. IEEE*, 2002, **90**, 1065–1076.
46 T. P. Chow and R. Tyagi, *IEEE Trans. Electron Devices*, 1994, **41**, 1481–1483.
47 J. Xing, E. Guo and H. Lu, *Sci. China: Phys., Mech. Astron.*, 2011, **54**, 1416–1419.
48 J. Seol, G. Lee and S. Hahm, *IEEE Sens. J.*, 2018, **18**, 4477–4481.
49 C. Chin-Hsiang, T. Yu-Hsuan, T. Sung-Yi and C. Chung-Fu, *Jpn. J. Appl. Phys.*, 2011, **50**, 04DG19.
50 I. E. Castelli, D. D. Landis, K. S. Thygesen, S. Dahl, I. Chorkendorff, T. F. Jaramillo and K. W. Jacobsen, *Energy Environ. Sci.*, 2012, **5**, 9034–9043.
51 S. Bruzzone and G. Fiori, *Appl. Phys. Lett.*, 2011, **99**, 222108.
52 S. Takagi, A. Toriumi, M. Iwase and H. Tango, *IEEE Trans. Electron Devices*, 1994, **41**, 2357–2362.
53 J. Qiao, X. Kong, Z.-X. Hu, F. Yang and W. Ji, *Nat. Commun.*, 2014, **5**, 4475.
54 Y. Guo, S. Zhou, J. Zhang, Y. Bai and J. Zhao, *2D Mater.*, 2016, **3**, 025008.
55 K. Kaasbjerg, K. S. Thygesen and A.-P. Jauho, *Phys. Rev. B: Condens. Matter Mater. Phys.*, 2013, **87**, 235312.
56 Z. Xie, S. Lin and Z. Wang, *Ceram. Int.*, 2018, **44**, 15912–15917.
57 Y.-F. Zhang, H. Ren and Z.-T. Hou, *J. Magn. Magn. Mater.*, 2015, **375**, 61–64.
58 D. Wang, Z.-P. Liu and W.-M. Yang, *ACS Catal.*, 2018, **8**, 7270–7278.
59 Z.-Y. Jiao, S.-H. Ma and J.-F. Yang, *Solid State Sci.*, 2011, **13**, 331–336.
60 F. Xia, H. Wang, D. Xiao, M. Dubey and A. Ramasubramaniam, *Nat. Photonics*, 2014, **8**, 899.
61 K. Watanabe, T. Taniguchi and H. Kanda, *Nat. Mater.*, 2004, **3**, 404.
62 J. Wang, H. Fang, X. Wang, X. Chen, W. Lu and W. Hu, *Small*, 2017, **13**, 1700894.
63 M. Sajjad, W. M. Jadwisienczak and P. Feng, *Nanoscale*, 2014, **6**, 4577–4582.
64 Y. Tao, X. Wu, W. Wang and J. Wang, *J. Mater. Chem. C*, 2015, **3**, 1347–1353.
65 J.-J. Wu, Y.-R. Tao, Y. Wu and X.-C. Wu, *Sens. Actuators, B*, 2016, **231**, 211–217.
66 W. Kohn and L. J. Sham, *Phys. Rev.*, 1965, **140**, A1133–A1138.
67 G. Kresse and J. Furthmüller, *Phys. Rev. B: Condens. Matter Mater. Phys.*, 1996, **54**, 11169–11186.
68 P. E. Blöchl, *Phys. Rev. B: Condens. Matter Mater. Phys.*, 1994, **50**, 17953–17979.
69 G. Kresse and D. Joubert, *Phys. Rev. B: Condens. Matter Mater. Phys.*, 1999, **59**, 1758–1775.
70 J. P. Perdew, K. Burke and M. Ernzerhof, *Phys. Rev. Lett.*, 1996, **77**, 3865–3868.
71 S. Grimme, J. Antony, S. Ehrlich and H. Krieg, *J. Chem. Phys.*, 2010, **132**, 154104.
72 A. Togo, F. Oba and I. Tanaka, *Phys. Rev. B: Condens. Matter Mater. Phys.*, 2008, **78**, 134106.
73 S. Baroni, S. de Gironcoli, A. Dal Corso and P. Giannozzi, *Rev. Mod. Phys.*, 2001, **73**, 515–562.
74 M. Acerce, D. Voiry and M. Chhowalla, *Nat. Nanotechnol.*, 2015, **10**, 313.
75 X. Fan, P. Xu, D. Zhou, Y. Sun, Y. C. Li, M. A. T. Nguyen, M. Terrones and T. E. Mallouk, *Nano Lett.*, 2015, **15**, 5956–5960.
76 Y. Wang, M. Miao, J. Lv, L. Zhu, K. Yin, H. Liu and Y. Ma, *J. Chem. Phys.*, 2012, **137**, 224108.
77 Y. Wang, J. Lv, L. Zhu and Y. Ma, *Phys. Rev. B: Condens. Matter Mater. Phys.*, 2010, **82**, 094116.
78 Y. Guo, Q. Wu, Y. Li, N. Lu, K. Mao, Y. Bai, J. Zhao, J. Wang and X. C. Zeng, *Nanoscale Horiz.*, 2019, DOI: 10.1039/c8nh00216a.
79 X. Luo, J. Yang, H. Liu, X. Wu, Y. Wang, Y. Ma, S. H. Wei, X. Gong and H. Xiang, *J. Am. Chem. Soc.*, 2011, **133**, 16285–16290.
80 V. S. Bhadram, H. Liu, E. Xu, T. Li, V. B. Prakapenka, R. Hrubiak, S. Lany and T. A. Strobel, *Phys. Rev. Mater.*, 2018, **2**, 011602.

